Wake flow pattern modified by small control cylinders at low Reynolds number

C.-H. Kuo*, L.-C. Chiou, C.-C. Chen

Department of Mechanical Engineering, National Chung Hsing University, No. 250 Kuo-Kuang Road, Taichung 40227, Taiwan

Abstract

Passive wake control behind a circular cylinder in uniform flow is studied by numerical simulation for Re_D ranging from 80 to 300. Two small control cylinders, with diameter $d/D = 1/8$, are placed at $x/D = 0.5$ and $y/D = \pm 0.6$. Unlike the 1990 results of Strykowski and Sreenivasan, in the present study, the vortex street behind the main cylinder still exists but the fluctuating lift and the form drag on the main cylinder reduces significantly and monotonously as the Reynolds number increases from 80 to 300. Obstruction of the control cylinders to the incoming flow deflects part of the fluid to pass through the gap between the main and control cylinders, forming two symmetric streams. These streams not only eliminate the flow separation along the rear surface of the main cylinder, they also merge toward the wake centerline to create an advancing momentum in the immediate near-wake region. These two effects significantly reduce the wake width behind the main cylinder and lead to monotonous decrease of the form drag as the Reynolds number increases. As the Reynolds number gets higher, a large amount of the downstream advancing momentum significantly delays the vortex formation farther downstream, leading to a more symmetric flow structure in the near-wake region of the main cylinder. As the Reynolds number increases from 80 to 300, both increasing symmetry of the flow structure in the near-wake and significant delay of the vortex formation are the main reasons for the fluctuating lift to decrease monotonously.
© 2007 Elsevier Ltd. All rights reserved.

Keywords: Passive wake control; Circular cylinder; Unsteady lift; Drag reduction; Vortex street

1. Introduction

Because of the practical importance of bluff bodies in uniform flow, a large number of numerical and experimental investigations have been performed for a wide range of Reynolds numbers (Griffin, 1995; Hoerner, 1957; Kim and Lee, 2001; Roshko, 1955; Suryanarayana et al., 1993). Details on the subject of a circular cylinder in uniform flow can also be found in the book of Zdravkovich (1997). Within a wide range of Reynolds numbers ($46 < Re_D < 2 \times 10^5$), wake flow patterns are complicated by factors such as turbulence intensity, aspect ratio, blockage ratio, end effects, wall proximity, etc. Although the Reynolds number is usually high in most practical situations, wake flows are also important at low Reynolds numbers for microsystem applications. Three important goals to modify the wake

*Corresponding author. Tel.: +886 422840433x314; fax: +886 422877170.
E-mail address: chkuo@dragon.nchu.edu.tw (C.-H. Kuo).

Nomenclature

C_D	drag coefficient
C_{dp}	form drag coefficient of the main cylinder
C_{dT}	total drag coefficient of a single cylinder or cylinder system
C_L	lift coefficient
$\langle C_L \rangle$	fluctuating amplitude of the lift coefficient
C_P	fluctuating surface pressure coefficient
D	diameter of the main cylinder (cm)
d	diameter of the control cylinder, $d/D = 1/8$
L_f	vortex formation length (cm)
L_d	vortex formation distance (cm)
Δr	grid size in radial direction
Re_D	Reynolds number, $\mathrm{Re}_D = \rho U_i D / \mu$
St_D	Strouhal number, $\mathrm{St}_D = fD/U_i$
S1	rear stagnation point on the main cylinder
S2, S3	four-way saddle points of the recirculation region
T_S	shedding period of vortex street (s)
t	time instant (s)
Δt	time increment (s)
U_{Bo}	mean velocity of reversed flow along wake centerline (cm/s)
$U_{Bo\max}$	maximum mean velocity of reversed flow at wake centerline (cm/s)
U_i	uniform inflow speed (cm/s)
$\bar{U}$	mean streamwise velocity (cm/s)
u	streamwise velocity (cm/s)

$\tilde{u}_{\mathrm{r.m.s.}}$	root-mean-square value of the velocity fluctuation (cm/s)
v	transverse velocity (cm/s)
x	streamwise coordinate
X_1	new streamwise coordinate centered at the saddle point S1 or S3
$X_{Bo\max}$	streamwise location corresponding to $U_{Bo\max}$
y	transverse coordinate
Y_1	new transverse coordinate centered at the saddle point S1 or S3
z	spanwise direction
θ	angle from the forward stagnation point of the main cylinder (deg)
$\Delta\theta$	circumferential angular increment (deg)
μ	viscosity (dyne s/cm^2)
ρ	density (g/cm^3)

Subscripts

o	refers to the condition without control cylinders
c	refers to the condition with control cylinders

Superscripts

*	refers to nondimensional quantities
Overbar	refers to the mean quantities

flows at low Reynolds numbers are: (i) reducing the form drag (Huner and Hussey, 1977; Suryanarayana et al., 1993), (ii) suppressing the vortex shedding (Bearman, 1965; Berger, 1967; Blevins, 1985; Strykowski and Sreenivasan, 1990), and (iii) changing the heat transfer characteristics (Lange et al., 1998).

Active and passive wake controls are usually employed in the literature. For the former, acoustics excitations (Blevins, 1985), heating the cylinder (Lecordier et al., 1991), oscillating the cylinder at an appropriate frequency or frequency-modulation (Berger, 1967; Nakano and Rockwell, 1991; Tokumaru and Dimotakis, 1991; Suryanarayana et al., 1993), blowing and suction (Bearman, 1965), and recently electromagnetic force control (Kim and Lee, 2001) are typical examples. For the latter, typical examples are surface protrusions (Nigim and Batill, 1997) to change the flow separation location, shrouds to affect the fluid entrainment (Zdravkovich, 1997), the rear-wake stabilizer to minimize the mutual interactions of separated shear layers (Bearman, 1965; Eisenlohr and Eckelmann, 1989), and recently use of a very small control cylinder to efficiently suppress the wake behind the main cylinder (Strykowski and Sreenivasan, 1990).

At Reynolds number less than 100, the experimental and numerical study of Strykowski and Sreenivasan (1990) showed complete wake suppression behind a circular cylinder by a very small control cylinder with diameter ratio $d/D = 20$. They further elucidated that damping out the temporal instability in the near-wake region is the primary reason for effective wake suppression. Their results showed that, at $\mathrm{Re}_D = 70$, a contoured region, located slightly above the mean loci of the maximum vorticity, can lead to effective wake suppression. The size of this contoured region will further reduce and move upstream toward the main cylinder when the Reynolds number increases from 46 to 80. So far, at higher Reynolds numbers ($\mathrm{Re}_D > 120$), the mechanisms for reducing the form drag and fluctuating lift or the possible wake control are still not clear. This inspires us to locate the control cylinders at $x/D = 0.5$ and $y/D = \pm 0.6$ with a hope to modify the wake behind the main cylinder or reduce the loading on the main cylinder at high Reynolds numbers. Therefore, the objective of this numerical study is to understand the wake flow structures modified by two small control cylinders placed at $x/D = 0.5$ and $y/D = \pm 0.6$ as the Reynolds number ranges from 80 to 300.

The format is organized in the following sequence. After the Introduction, the physical system considered is described in Section 2. The problem formulation describing the governing equations, associated with proper boundary and initial conditions, as well as the numerical methods, are stated in Section 3. Also, validations of the present simulation model are performed in that section. Results and discussion are given in Section 4. Finally, a conclusion under specific flow conditions is given.

2. Physical system

In Fig. 1, the center of main cylinder with diameter D is defined as the origin of the flow domain with uniform inflow velocity (U_i) entering from the left boundary. Two small control cylinders, having diameter $d/D = 1/8$, are placed at two symmetric locations about the wake centerline (e.g., at $x/D = 0.5$ and $y/D = \pm 0.6$). The flow domain is divided into several blocks with multiple mesh densities to satisfy the local resolution in the flow of large velocity gradient. The total number of grid point is around 3×10^5. The surface of the main cylinder is discretized into a total of 300 control volumes (CV) at the finest level, leading to a circumferential resolution of $\Delta\theta = 1.2°$. In the radial direction, the smallest grid size is about $\Delta r/D = 2 \times 10^{-3}$.

To ensure that the limited computational domain does not affect the solution, the upper and the lower-most boundaries are located far away from the main cylinder at $y/D = \pm 25$. In Fig. 1, the leftmost and the rightmost boundaries of the flow domain are located at $x/D = -10$ and 40, respectively. Any further extension of the flow domain in both x and y directions yields the same flow velocity and surface pressure distributions, with maximum deviation about 0.21% and 1.57%, respectively. Therefore, to compromise both the computation efficiency and the accurate results, the flow domain is employed as depicted in Fig. 1 for all the cases investigated herein.

3. Problem formulations and model validations

3.1. Governing equation

For an unsteady, two-dimensional, laminar and incompressible fluid flow with constant properties, the nondimensional continuity and momentum equations in Cartesian coordinate can be expressed in tensor forms as

$$\partial u_i^* / \partial x_i^* = 0, \quad i = 1, 2, \tag{1}$$
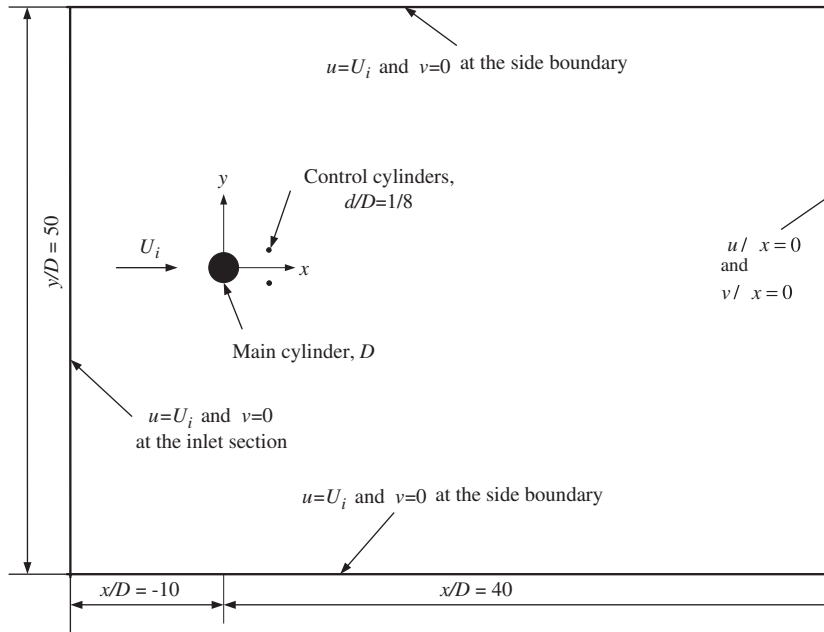

Fig. 1. Coordinate system of the main and the control cylinders, flow boundaries of the simulation domain and the boundary conditions specified. The control cylinders are placed at $x/D = 0.5$ and $y/D = \pm 0.6$ for $Re_D = 80$–300.

$$\partial u_i^*/\partial t^* + \partial(u_i^* u_j^*)/\partial x_j^* = -\partial p^*/\partial x_i^* + (2/\mathrm{Re}_D)\partial^2 u_i^*/\partial x_j^* \partial x_j^*, \quad i,j = 1,2. \tag{2}$$

Velocities, pressure and spatial coordinates in Eqs. (1) and (2) are nondimensionalized by the free-stream velocity U_i, velocity head $\rho U_i^2/2$ and the radius of the main cylinder $D/2$, respectively. The set of coupled differential equations will be solved by the large eddy simulation (LES) method for the unknown pressure p, and the two velocity components (u_i, $i = 1, 2$) in x and y directions. The gravity force is excluded in the present study. The computations are carried out by the Fluent (2005) solver based on the finite volume method with quadrilateral differential CV. All the dependent variables are located at the center of each CV. Values of the velocity components and the pressure at the CV face locations are expressed in terms of nodal values using a central differencing scheme. Thus, the present scheme has a second-order spatial accuracy.

For calculation of pressure, a pressure-correction equation based on the SIMPLER algorithm (Patankar and Spalding, 1972) is employed. For details on the discretization and the pressure–velocity coupling, refer to Ferziger and Peric (1996). The iteration process stops as long as the sum of the absolute residuals in all equations is less than 10^{-4}. This convergence criterion considers the balance between the accuracy near the wall, and the shear layer as well as the computational efficiency. All the final results are tested to be independent of the initial conditions and the number of grid points.

3.2. Boundary condition

The no-slip boundary conditions are assigned on the surfaces of the main and the control cylinders, as follows:
Inflow boundary condition:

$$u = U_i \text{ and } v = 0, \quad \text{at } x/D = -10 \text{ for } -25 \leqslant y/D \leqslant 25, \tag{3}$$

outflow boundary condition:

$$\partial u/\partial x = 0 \text{ and } \partial v/\partial x = 0, \quad \text{at } x/D = 40 \text{ for } -25 \leqslant y/D \leqslant 25, \tag{4}$$

the upper and the lower boundary conditions:

$$u = U_i \text{ and } v = 0, \text{ at } y/D = \pm 25 \text{ for } -10 \leqslant x/D \leqslant 40. \tag{5}$$

The initial velocities in the flow domain are specified as $u = U_i$ and $v = 0$ at $t = 0$. In case of unsteady flow calculations, suitable time steps and the modified Crank–Nicolson scheme are employed. The nondimensional time step is selected as $\Delta t^* = U_i \Delta t/D = 10^{-4}$ in the first 40 s, $\Delta t^* = 10^{-3}$ for the next 20 s and finally $\Delta t^* = 10^{-2}$ in order to avoid the nonphysical oscillations and obtain a smooth time-dependent solution.

3.3. Validation of simulation model

In Fig. 2, the dimensionless streamwise mean velocity profiles $U^*(= \bar{U}/U_i)$ obtained by simulation and experiment are compared at selected x/D locations behind a single cylinder for the same Reynolds number ($\mathrm{Re}_D = 80$). The measured velocities are obtained by a laser Doppler velocimetry (LDV) system in the plane at mid-span (at $z = 0$). In this experiment, the blockage ratio of the cylinder in the test-section is 6.7%. Details on the principle of the LDV system and the data acquisition system can be found in Kuo and Jeng (2003). Evidently, in the region $0.52 \leqslant x/D \leqslant 5.98$ and $-3 \leqslant y/D \leqslant 3$ of Fig. 2, the streamwise mean velocity profiles match well with the measured results, except for the overshoot along the separated shear layer in the immediate near-wake region. These deviations are caused by the differences in the blockage ratio between the simulated (2%) and experimental models (6.7%).

In Fig. 3, the instantaneous vorticity contours are shown within the flow domain $y/D = \pm 2.5$ and $-1 \leqslant x/D \leqslant 14$ at selected instants over the shedding cycle. Here $t^* = 0$ represents the dimensionless instant at which the upper vortex (V_2) is about to be shed downstream. The classical Karman vortex street sheds periodically downstream having a shedding frequency corresponding to $\mathrm{St}_D = 0.156$. Besides, other results obtained by simulation match quite well with the previously quoted literature in the bracket for a single cylinder around $\mathrm{Re}_D = 80$. For example, the form drag coefficient is calculated around 1.52 (Huner and Hussey, 1977; Roussopoulos, 1993). The Strouhal numbers of the fluctuating lift and drag on the cylinder are 0.156 and 0.312, respectively (Williamson and Brown, 1998). The simulated results also match quite well with those of Figures 11 and 22 in Strykowski and Sreenivasan (1990). Namely, around $\mathrm{Re}_D = 80$, the shedding frequency in terms of fD^2/ν gives a value 12.48. Besides, in the present study, the peak value of $\tilde{u}_{\mathrm{r.m.s.}}(0.27\% U_i)$ obtained at $y/D = 0.5$ and $\mathrm{Re}_D = 80$ is slightly higher than that measured at $y/D = 0.7$ and $\mathrm{Re}_D = 78$ in Strykowski and Sreenivasan (1990).
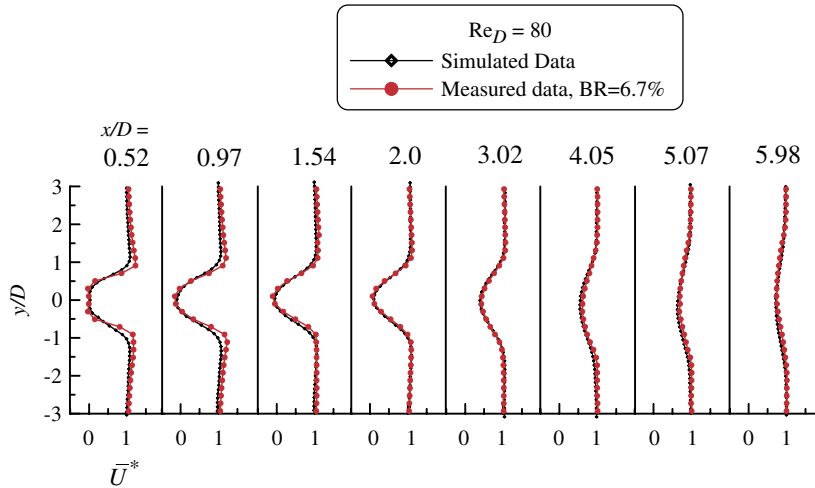
Fig. 2. Comparison of the measured and the simulated velocity profiles at several x/D locations behind a single cylinder at $Re_D = 80$. Note that the deviations of the overshoot region in the near wake are caused by different blockage ratios between the simulated and experimental models.
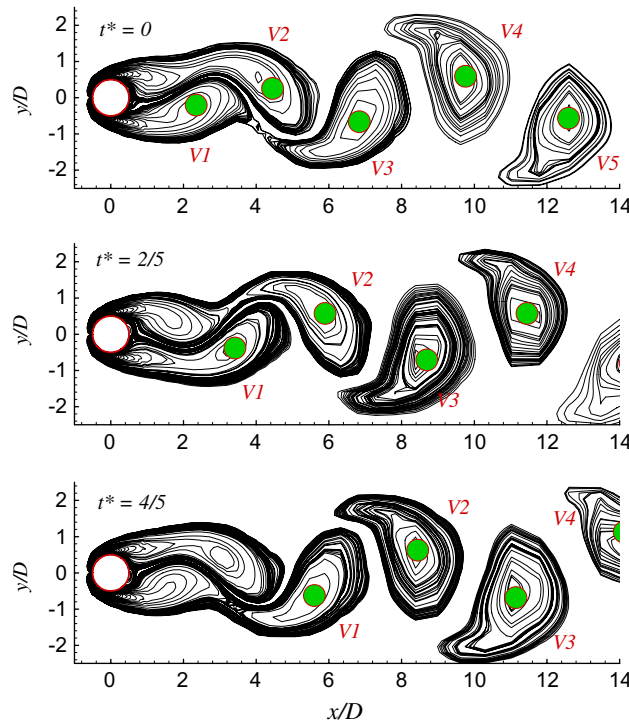

Fig. 3. Vorticity contours behind the main cylinder at selected instants within the shedding cycle without control cylinders at $Re_D = 80$. Note that $t^* = 0$ denotes the instant at which the upper vortex V_2 is about to be shed downstream.

Further examination of this simulated model has also been used to validate some of the results of Strykowski and Sreenivasan (1990) around $Re_D = 80$. For example, in Fig. 4(a), as only one small control cylinder with $d/D = 1/4$ is placed asymmetrically at $x/D = 1.53$ and $y/D = 1.1$, the streamline pattern behind the main cylinder exhibits two asymmetric stationary eddies, indicating complete suppression of the vortex street behind the main cylinder. In Fig. 4(b), when two control cylinders are placed symmetrically in the region of complete wake suppression, the
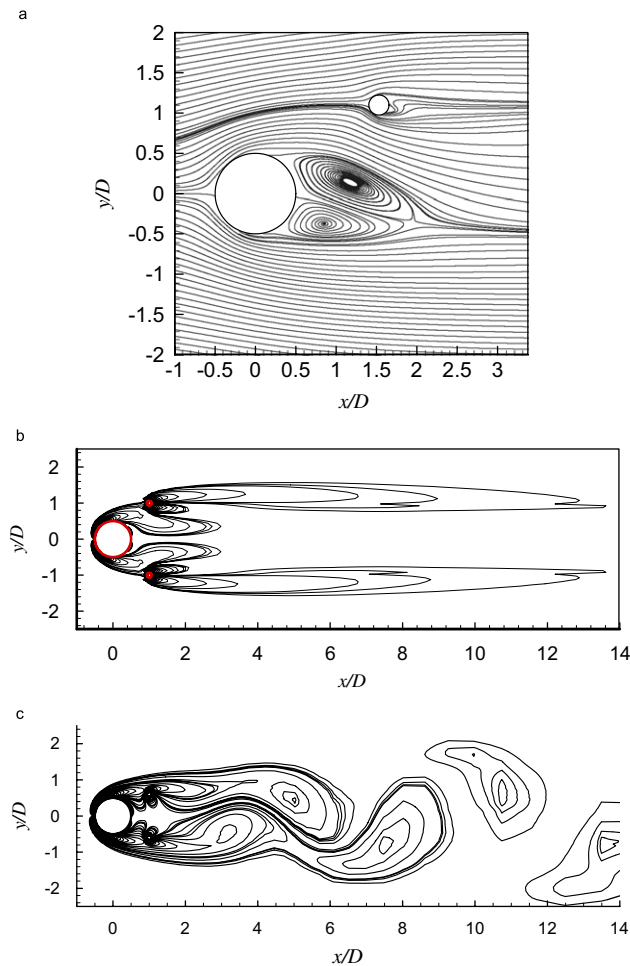
Fig. 4. (a) Instantaneous streamline pattern with one control cylinder ($d = D/4$) placed at $x/D = 1.53$ and $y/D = 1.1$; (b) instantaneous vorticity contours around the main cylinder when two control cylinders ($d = D/8$) are placed symmetrically at $x/D = 1.0$ and $y/D = \pm 1.0$; (c) two control cylinders are placed at $x/D = 0.8$ and $y/D = \pm 0.6$. All the Reynolds number are $\mathrm{Re}_D = 80$.

instantaneous vorticity contours are distributed symmetrically and do not vary with time. However, the Karman vortex street reappears in Fig. 4(c) when the control cylinders are placed outside the region of complete wake suppression. Compared with those illustrated in Fig. 5 of Strykowski and Sreenivasan (1990), the results depicted in Fig. 4 further confirm the simulation model used in the present study. Based on these preliminary validations, this simulation model will be employed to study the wake flow structures modified by two small control cylinders at Reynolds number ranging from 80 to 300.

4. Results and discussions

4.1. Flow characteristics at Reynolds number 80

When two small control cylinders ($d = D/8$) are placed symmetrically at $x/D = 0.5$ and $y/D = \pm 0.6$, the instantaneous vorticity contours over the same flow domain are depicted in Fig. 5(a). Compared with those in Fig. 3, the staggered vortex street behind the main cylinder in Fig. 5(a) still exists with slightly longer wavelength and lower Strouhal number. In other words, the periodic vortex shedding is only slightly affected by the control cylinders at Reynolds number 80. Though this result is largely different from the 40% frequency reduction found by Strykowski and

Sreenivasan (1990), there is no contradiction at all, because the location of the control cylinders in the present study is not located in the region where the wake is effectively suppressed. Furthermore, there exists a region of low vorticity (or vorticity depletion region) in the near-wake immediately behind the main cylinder.

Detailed velocity vectors and the associated streamline patterns in the near-wake region are shown in Fig. 5(b) within the shedding cycle. In Fig. 5(b) (left column), two saddle points (solid circles) wandering around $\theta = \pm135°$ denote the unsteady boundary layer separation near the rear surface of the main cylinder. Besides, the instantaneous alleyways in the near-wake penetrate alternately across the wake centerline, clearly indicating the shedding vortex street (Perry et al., 1982). However, in Fig. 5(c) (right column), all the velocity vectors in the gap between the main and the control cylinders move downstream, showing no flow reversal within the shedding cycle. Relative to the results in Fig. 5(b), this indicates that the flow vectors reverse their directions near the saddle point S1. In addition, there exists an extra four-way saddle point S3 in the near-wake region.

For a single cylinder in a uniform stream, contours of the streamline pattern, moving with the shedding vortex streets, are shown in Fig. 6(a) within the same flow domain as in Fig. 3. It is clear that, in Fig. 6(a), the locations of the well-defined centers in the far-wake region ($x/D > 5$) match well with those of the vorticity contours in Fig. 3. In the far-wake region, the already shed vortices move at nearly constant convection velocity and thus form the well-defined centers in the streamline patterns when observed in the frame moving with the shedding vortices (Perry et al., 1982). In the present study, the convective speed of the vortex street is evaluated at $x/D = 10$ where it becomes nearly constant and approximately equals $0.87U_i$. This value is very close to that obtained by Zhou and Antonia (1992) who claimed a convection velocity $0.84U_i \sim 0.86U_i$ in the far-wake region and that it is also independent of Reynolds number for the laminar wake. In the near-wake region of Fig. 6(a), the shape of contours is severely distorted. Because the vortices are at the formation stage in the near-wake region, the centers of the distorted vortices are shifted to different extents and move at a much lower speed than those of the shedding vortices.
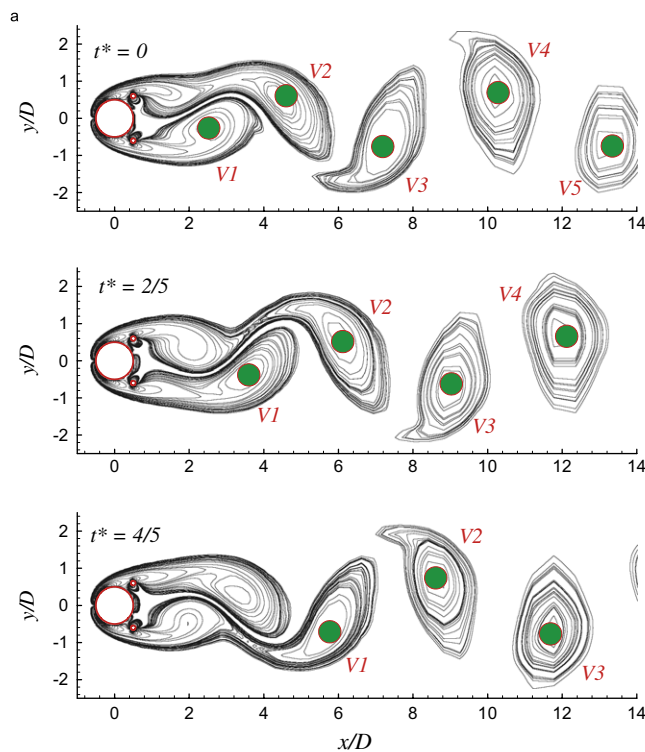

Fig. 5. (a) Vorticity contours behind the main cylinder, (b) velocity vectors and associated streamlines in the near-wake region for the case without control cylinders, (c) velocity vectors and associated streamlines in the near-wake region with control cylinders at selected instants within the shedding cycle for $Re_D = 80$. Note that $t^* = 0$ denotes the instant at which the upper vortex V_2 is about to be shed downstream. The solid circles represent the saddle points and the hollow circles denote the small control cylinders located at $x/D = 0.5$ and $y/D = \pm0.6$.
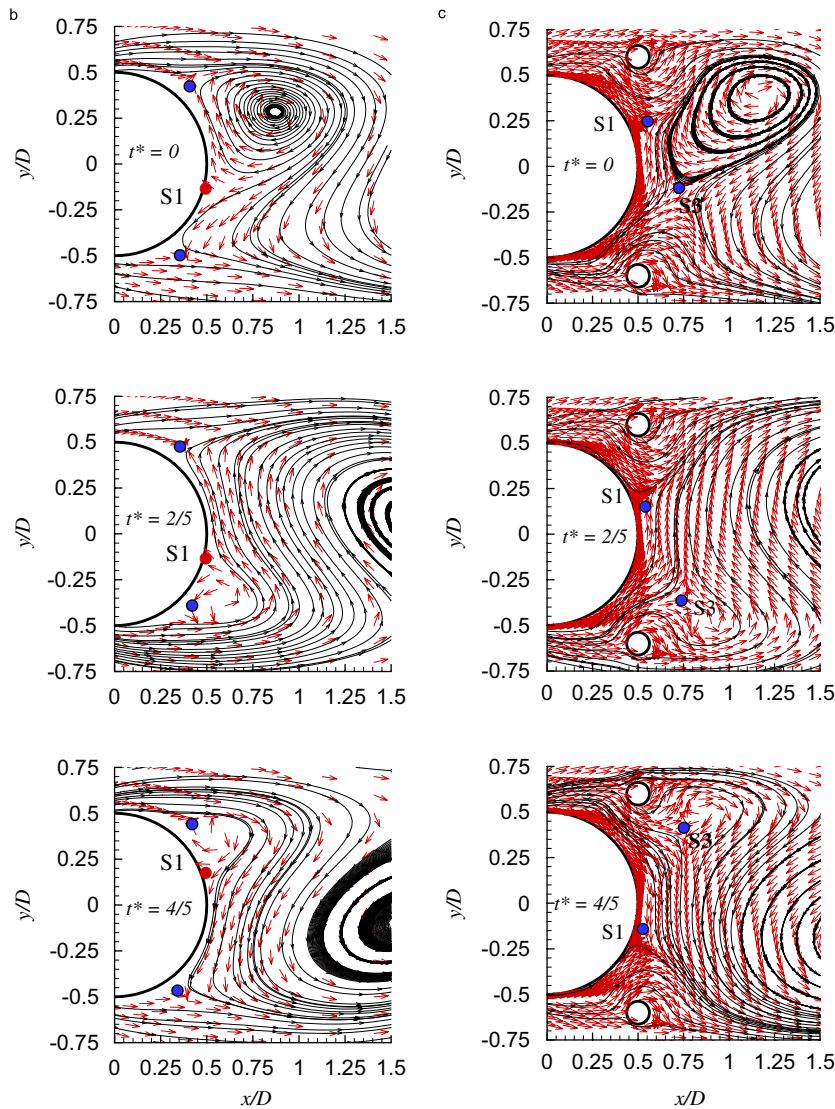
Fig. 5. (*Continued*)

In Fig. 6(b), the mean streamline pattern, averaged over ten vortex shedding cycles, shows two recirculation regions located symmetrically about the wake centerline ($y/D = 0$). The recirculation region is bounded streamwisely by two saddle points S1 and S2. The three-way saddle point S1 represents the mean location of the instantaneous rear stagnation point of the main cylinder in Fig. 5(b); while the four-way saddle point S2 represents the mean location of the instantaneous four-way saddle point S2 in the near-wake region of Fig. 6(a). From Figs. 3, 6(a) and (b), it is clear that the region between S1 and S2 provides a streamwise space for vortex formation before it starts to shed downstream. The vortex shedding will occur downstream of the saddle point S2.

The mean streamline pattern around the main cylinder with two control cylinders is depicted in Fig. 6(c). Evidently, the streamlines, passing through the gap, follow the rear surface profile ($90° \leqslant \theta \leqslant 180°$) of the main cylinder, and converge toward S1. Subsequently, the streamlines neck symmetrically toward the wake centerline and an extra saddle point S3 is formed in the near-wake region of Fig. 6(c). The four-way saddle point S2 is now located at $x/D = 2.6$, showing a 30% elongation or downstream delay relative to that in Fig. 6(b).

It is clear in Fig. 5(c) that obstruction of the control cylinders to the incoming flow deflects part of the fluid to pass through the gaps between the main and the control cylinders without flow reversal. In Fig. 6(c), necking of the streamlines in the immediate near-wake is primarily caused by the merging of the two streams toward the wake
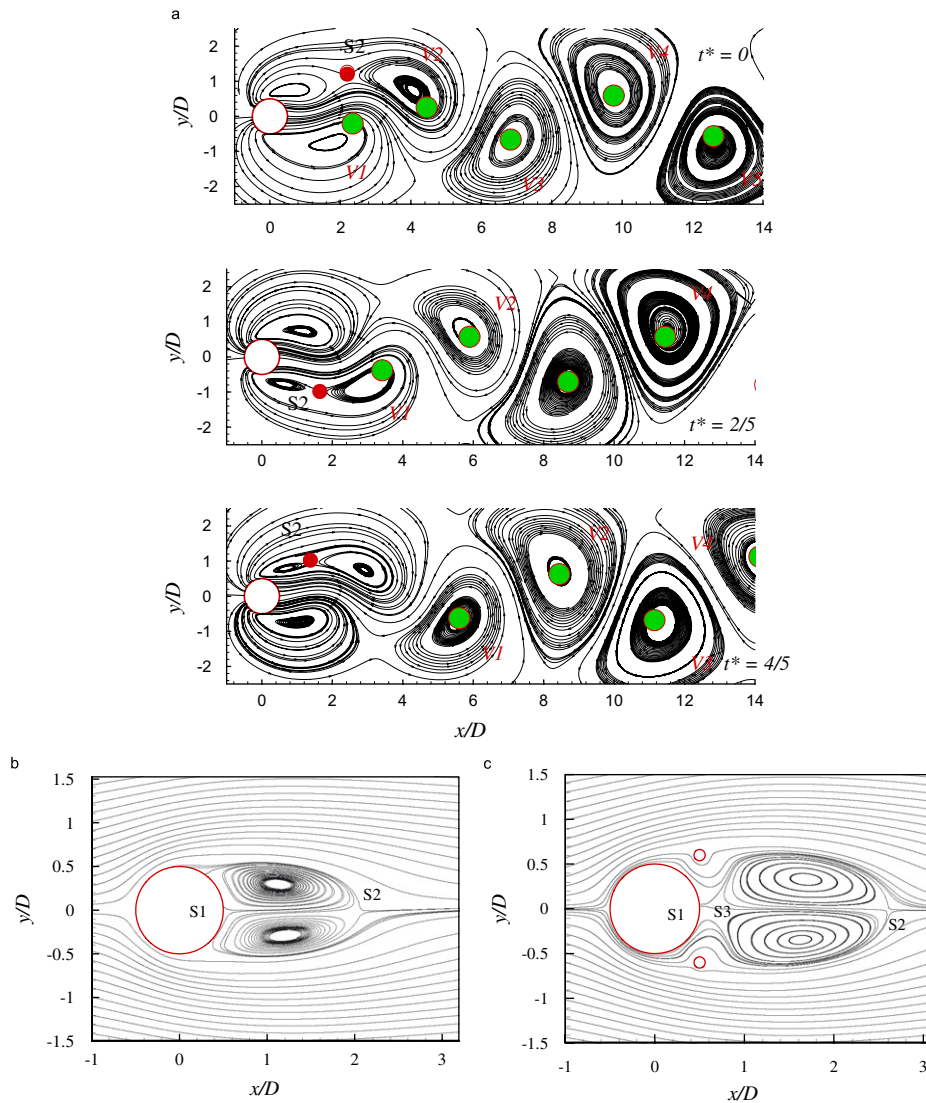
Fig. 6. (a) Instantaneous streamline patterns, (b) contours of mean streamlines without control cylinders, (c) contours of mean streamlines with two control cylinders at $Re_D = 80$. Note that the instantaneous streamline patterns are observed in the coordinate moving with the shedding vortex for $Re_D = 80$.

centerline. In fact, the merging streams create extra advancing momentum in the downstream direction, forming a new saddle point S3 in the near-wake region. In Fig. 6(c), the extra saddle point S3, formed very close to the main cylinder, is due to the small amount of the advancing momentum at Reynolds number 80. It is clear that the downstream advancing momentum delays not only the vortex formation region but also the location of the vortex shedding from the main cylinder.

4.2. Reynolds number effects

4.2.1. Vorticity contours

As the Reynolds number changes from 120 to 300, the vorticity contours behind a single cylinder show similar dynamic characteristics as those in Fig. 3, except that the early rolling up of the first vortex means a shorter wavelength of the vortex street. In addition, the Strouhal number changes from 0.176 to 0.20 (Williamson and Brown, 1998) and 0.212 as the Reynolds number varies from 120 to 300.
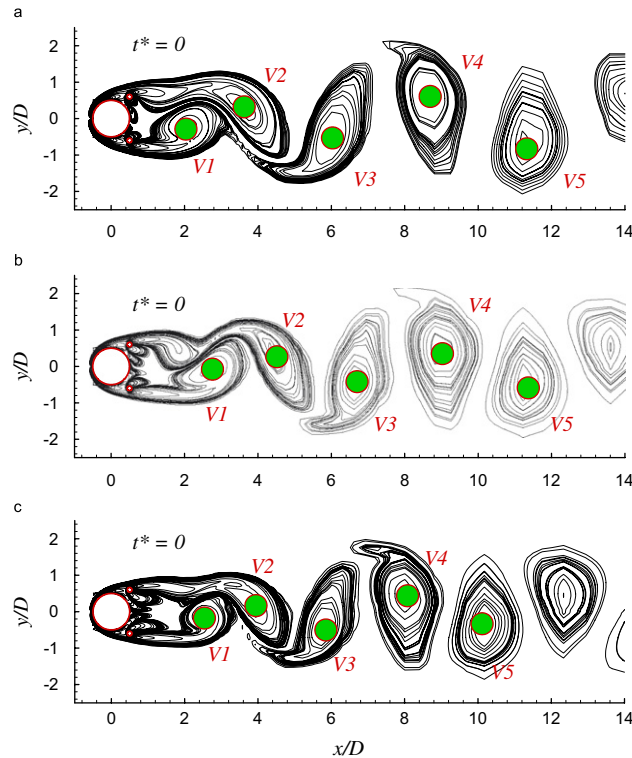
Fig. 7. Vorticity contours behind the main cylinder at the instants $t^* = 0$ for $Re_D =$ (a) 120, (b) 220 and (c) 300 when two control cylinders are located at $x/D = 0.5$ and $y/D = \pm 0.5$.

When the control cylinders are placed at $x/D = 0.5$ and $y/D = \pm 0.6$, the vorticity contours at the instant $t^* = 0$ are shown in Fig. 7 for $Re_D = 120$–300. Evidently, the periodic shedding vortex street still remains. However, the wavelength is reduced and the Strouhal numbers of the shedding vortex streets increase from 0.172 to 0.195 and 0.207 as the Reynolds number increases. In Fig. 7, there also exists a vorticity depletion (or low vorticity) region in the immediate near wake of the main cylinder. The vorticity depletion region gets longer as the Reynolds number increases from 120 to 300. Furthermore, immediately behind the control cylinders, two small regions with intensive vorticity levels are getting more symmetric about the wake centerline as the Reynolds number increases from 120 to 300.

4.2.2. Near-wake flow structures

To get further insight of the near-wake flow structures, the velocity vectors and the associated streamline patterns are depicted in Fig. 8. For the cases without control cylinders, some similarities are found in Fig. 8(a) (left column). For example, there are two saddle points (solid circles) wandering near $\theta = \pm 135°$, indicating the existence of unsteady flow separation from the main cylinder. Similarly, the highly curved alleyways cross the wake centerline and change their directions alternately within the shedding cycle, indicating the periodically shedding vortex streets.

For all Reynolds numbers in Fig. 8(b) (right column), some differences should be noticed relative to the no-control counterpart (Fig. 8(a)). First of all, the velocity vectors in the gap region move along the rear surface of the main cylinder, indicating no flow separation within the gap. Secondly, two streams through the gap flow along the rear surface of the main cylinder and merge near S1. Note that all the velocity vectors change directions near S1. Third, two merging streams through the gap create an advancing momentum in the downstream direction. This advancing momentum further alleviates the degree of rotation (or levels of vorticity), leading to a vorticity depletion regime in the immediate near-wake region. Fourth, the near-wake flow structure becomes more symmetric about the wake centerline as the Reynolds number increases.

In Fig. 7, the intensive levels of the vorticity contours behind the small control cylinders and near the rear surface of the main cylinder are the result of large velocity gradient of the streams passing through the gap.
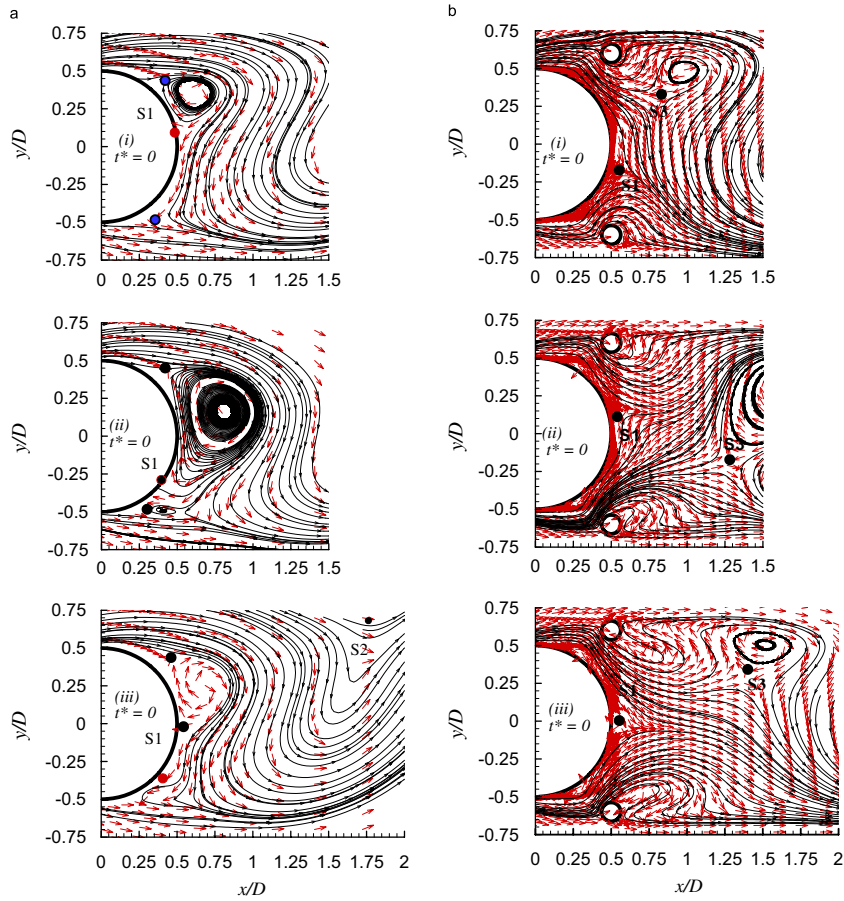
Fig. 8. Velocity vectors and associated streamlines in the near-wake region of the main cylinder at the instants $t^* = 0$ for three Reynolds numbers, Re_D = (i) 120, (ii) 220 and (iii) 300: (a) without control cylinders; (b) with two control cylinders.

4.2.3. Mean streamline patterns

The mean streamline patterns are illustrated in Fig. 9 to compare the flow topology at different Reynolds numbers for cases with and without the control cylinders. On the left column of Fig. 9, the saddle point S2 moves upstream toward the main cylinder and the streamwise distance between S1 and S2 becomes shorter as the Reynolds number increases. When two control cylinders are placed at $x/D = 0.5$ and $y/D = \pm 0.6$ (right column of Fig. 9), the saddle point S1 still remains at the same location on the main cylinder, and a new saddle point S3 is formed in the near wake. The saddle point S3 is delayed significantly downstream, whereas the location of S2 is delayed downstream only slightly. It is clear that, as the Reynolds number increases from 120 to 300, the merged flow in the near-wake region creates an increasing amount of the advancing momentum in the downstream direction. The enhanced advancing momentum in the near-wake region leads to elongated necking of the streamlines and significant downstream movement of S3 location. It also shifts the recirculation region farther downstream and reduces the size of the recirculation region. Obviously, as the Reynolds number increases, the enhanced advancing momentum also alleviates the rotation rate of the fluid (or reunifies the flow directions) in the near-wake region. Therefore, the advancing momentum is primarily responsible for the elongated region of the vorticity depletion in the near-wake region (Fig. 7).

4.3. Root-mean-squared value of the velocity fluctuation

Apart from the unsteady characteristics (e.g., vorticity contours, streamline patterns and the velocity vectors), contours and streamwise variations of $\tilde{u}_{r.m.s.}$ at various Reynolds numbers are also illustrated in Fig. 10 for the cases with and without control cylinders. The magnitudes of $\tilde{u}_{r.m.s.}$ in the flow domain are calculated by Eq. (6) over ten
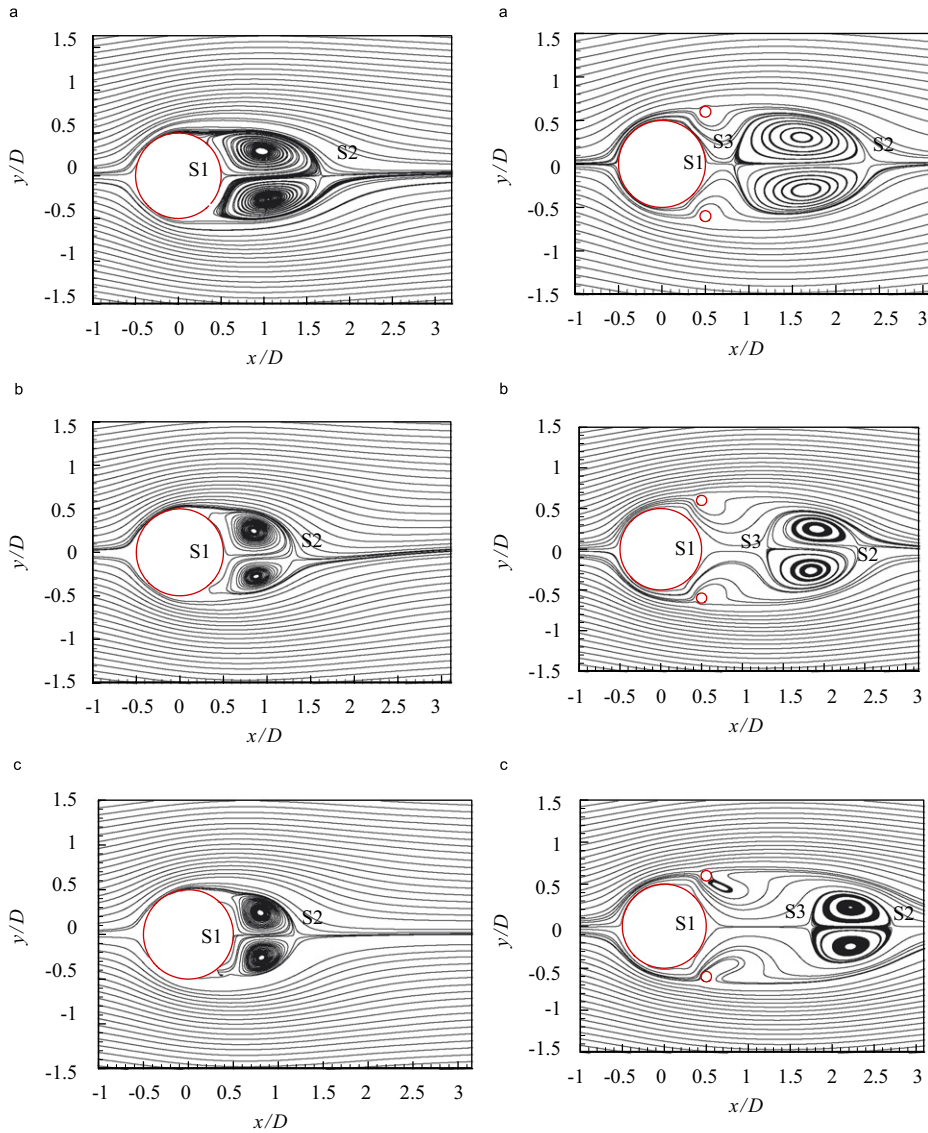
Fig. 9. Contours of mean streamline patterns behind the main cylinder at three Reynolds numbers, $Re_D =$ (a) 120, (b) 220 and (c) 300. The left column is for the cases without control cylinders; the right column represents the cases with two control cylinders.

vortex shedding cycles (T_s):

$$\tilde{u}_{\text{r.m.s.}} = \left\{ \sqrt{\int_0^{10T_S} [u(t) - \bar{U}]^2 \, dt} \right\} \Big/ 10T_S. \tag{6}$$

In Fig. 10, all the contours of $\tilde{u}_{\text{r.m.s.}}$ are distributed symmetrically about the wake centerline. All these contour distributions agree well with the eigenmodes of $\tilde{u}(t)$ predicted by linear stability analysis. In Fig. 10(a), the locations of peak $\tilde{u}_{\text{r.m.s.}}$ move upstream toward the main cylinder as the Reynolds number increases from 120 to 300. This trend agrees well with the results of Bearman (1965). However, the peak locations of $\tilde{u}_{\text{r.m.s.}}$ are situated farther downstream in Fig. 10(b) than those in Fig. 10(a). Similar eigenmodes of $\tilde{u}(t)$ in Fig. 10(a) and (b) imply that the vortex street still remains in the far-wake. Besides, in the immediate near-wake region of Fig. 10(b), the regions of low $\tilde{u}_{\text{r.m.s.}}$ values are actually associated with the vorticity depletion regions shown in the corresponding vorticity contours.
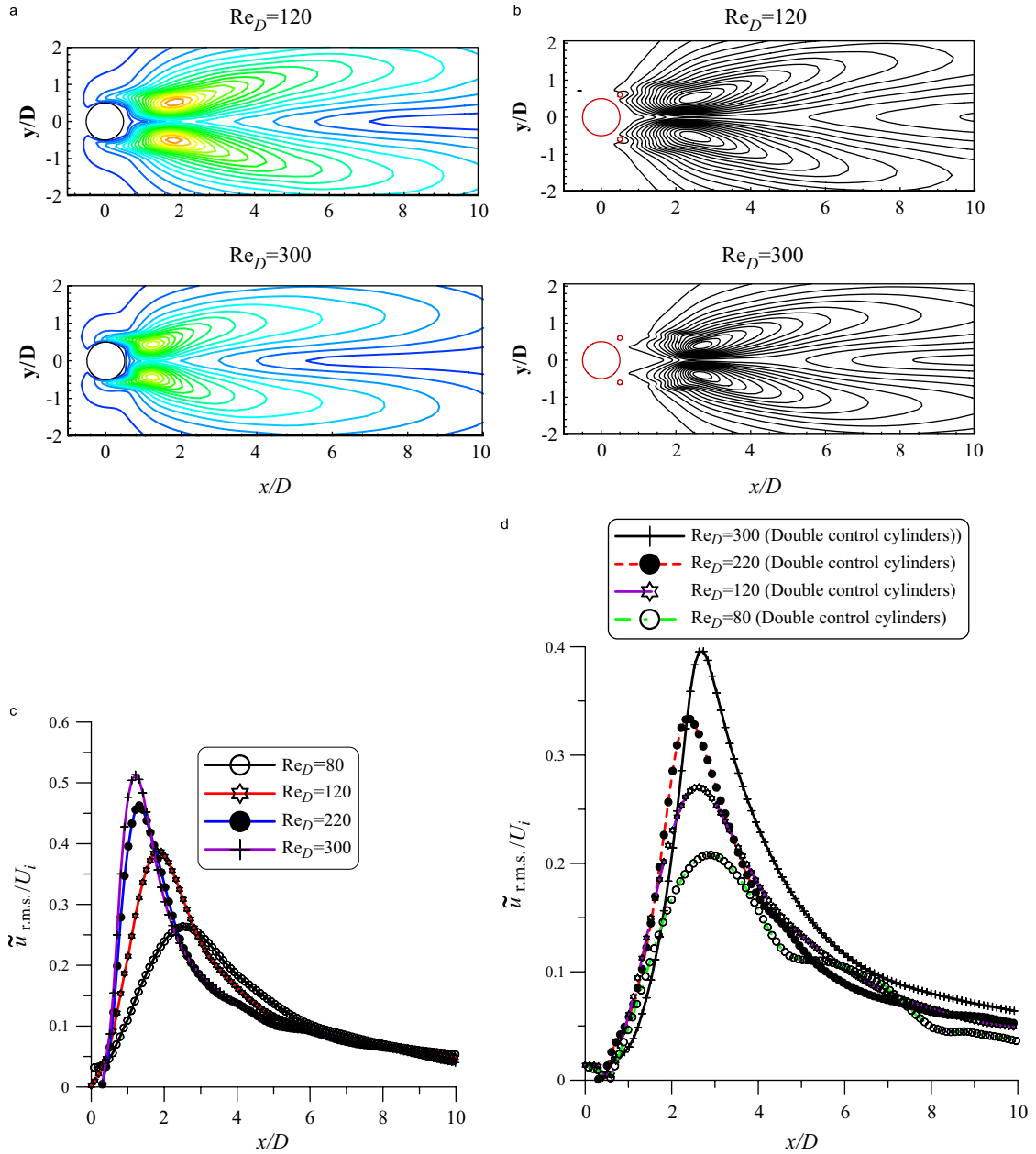
Fig. 10. Contour distributions and streamwise variations of the $\tilde{u}_{r.m.s.}$ at different Reynolds numbers. (a, c) Without control cylinders and (b, d) with two control cylinders.

Streamwise variations of $\tilde{u}_{r.m.s.}$ along an elevation $y/D = 0.5$ are shown in Fig. 10(c) and (d) to illustrate the growth and the decay of $\tilde{u}_{r.m.s.}$ along the separating shear layer. The peak value of $\tilde{u}_{r.m.s.}$ increases and the peak location of $\tilde{u}_{r.m.s.}$ moves upstream as the Reynolds numbers become higher for all the cases with and without control cylinders. However, the peak values of $\tilde{u}_{r.m.s.}$ are smaller in Fig. 10(d) than those in Fig. 10(c).

4.4. Surface pressure distributions

As the Reynolds number increases from 80 to 300, the distribution of the fluctuating surface pressure coefficient (C_p) are plotted in Fig. 11 at instant $t^* = 0$ for the cases with and without control cylinders. Note that $t^* = 0$ represents the
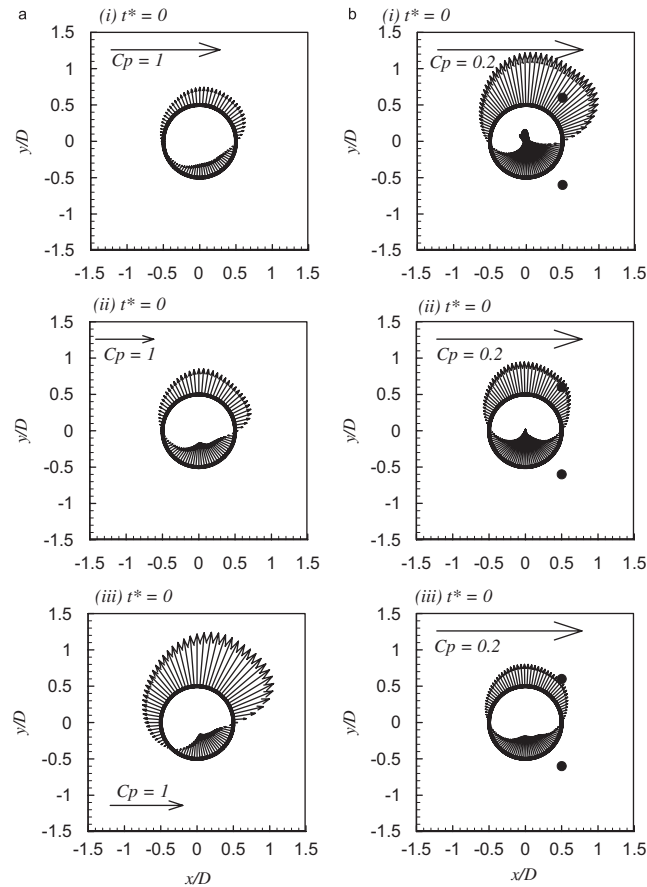
Fig. 11. Distributions of fluctuating pressure coefficient (C_p) on the surface of the main cylinder at $t^* = 0$ for different Reynolds numbers, $Re_D =$ (i) 80, (ii) 220 and (iii) 300: (a) without control cylinder; (b) with two control cylinders (solid circles). Note that the scales in (a) and (b) are greatly different.

instant when the vortex V_2 is about to shed downstream (Fig. 3). Fluctuating pressure coefficients are calculated by subtracting the mean surface pressure distribution on the main cylinder. Here the inward-pointed and the outward-pointed vectors denote the positive (or compression) and the negative (or suction) pressures on the main cylinder, respectively. Besides, the length of each vector (or arrow) indicates the magnitude of C_p. It is clear in Fig. 11(a) that the magnitude of C_p increases with increasing Reynolds number. The increasing magnitudes of C_p in Fig. 11(a) are in accordance with the increasing peak values of $\tilde{u}_{r.m.s.}$ in Fig. 10(c) as the Reynolds number increases from 80 to 300. On the other hand, in Fig. 11(b), as two control cylinders are placed at $x/D = 0.5$ and $y/D = \pm 0.6$, the magnitudes of C_p have maximum value at $Re_D = 80$ and decrease monotonously as the Reynolds number increases. Note the scales in Fig. 11(a) and (b) are quite different.

4.5. Lift variations as function of Reynolds number

To illustrate the efficiency of wake control, the fluctuating amplitudes of lift coefficient $\langle C_L \rangle$ on the main cylinder with and without control cylinders are shown in Fig. 12. Integration of the surface pressure distribution in the y-direction over a complete shedding cycle gives a cyclic variation of lift force on the main cylinder. It is clear in Fig. 12 that the fluctuating amplitude $\langle C_L \rangle$ without control cylinders increases monotonously with increasing Reynolds number. This trend is in accordance with the increasing magnitudes of $\tilde{u}_{r.m.s.}$ in Fig. 10(c) and C_p in Fig. 11(a) as the Reynolds number increases from 80 to 300. However, in Fig. 12(b), the fluctuating amplitude $\langle C_L \rangle$ decreases monotonously as Reynolds number increases. This variation agrees well with decreasing magnitudes of C_p in Fig. 11(b) as the Reynolds number increases from 80 to 300.

At $Re_D = 80$, the fluctuating amplitude of the lift coefficients $\langle C_L \rangle$ are comparable for the cases with and without control cylinders, implying only limited control efficiency. The inefficient wake control at $Re_D = 80$ is due to the fact that the control cylinders are placed outside and relatively far away from the complete wake suppression region. However, at higher Reynolds number, the control efficiency is greatly improved. The primary reason is due to different extents of flow-structure modification described in the previous section. From another viewpoint, the contoured region of complete wake suppression shrinks its size and moves close to the main cylinder, located slightly above the mean loci of the maximum vorticity, as the Reynolds number increases from 46 to 100 (Strykowski and Sreenivasan, 1990). The remarkable efficiency of wake control at high Reynolds number may also be caused by the fact that the control cylinders are placed relatively close to the complete wake suppression region. In the present study, the control cylinders are fixed at $x/D = 0.5$ and $y/D = \pm 0.5$ for all Reynolds numbers.

4.6. Drag variations as function of Reynolds number

In this section, all the form and the total drags are referred to the mean values. Fig. 13 depicts the variations of the form drag and the total drag (form drag plus viscous drag) coefficients at different Reynolds numbers. The form drag is obtained by integrating the normal pressure distribution in the x direction over the surface of the main cylinder. However, the total drag is calculated by the finite CV analysis. Here the CV is bounded by the region $-10 \leqslant x/D \leqslant 25$ and $-25 \leqslant y/D \leqslant 25$. Along the control surfaces, the mean static pressure and two mean velocity components are employed to perform this analysis. Further enlargement of the CV leads to only 1.6% deviation on the total drag.

In Fig. 13, the form drag coefficient ($\bar{C}_{dpo}$) of a single cylinder remains nearly constant around 1.51 for all the Reynolds numbers studied herein. These values are close to the results in previous literature (Kim and Lee, 2001; Lange et al., 1998; Williamson and Brown, 1998; Zdarvkovich, 1977). However, when two control cylinders are placed at $x/D = 0.5$ and $y/D = \pm 0.6$, the form drag coefficient ($\bar{C}_{dpc}$) of the main cylinder reduces monotonously as the Reynolds number increases from 80 to 300. It is evident from the velocity vectors and the associated streamline patterns in the near wake (Figs. 5(c) and 8(b)) that the flow passing through the gap completely eliminates the flow separation along the rear surface of the main cylinder for all Reynolds number studied herein. Both complete removal of flow separation and merging of two gap flows toward the wake centerline significantly reduce the wake width behind the main cylinder, and are the main reasons for monotonous reduction of the form drag for the cases with two control cylinders.

For a single main cylinder, the total drag coefficient ($\bar{C}_{dTo}$) starts from 1.78 at $Re_D = 80$ and increases mildly with increasing Reynolds numbers. The viscous drag is defined as the difference between the total drag and the form drag. In Fig. 13, the viscous drag coefficients (i.e. the difference of symbols ◆ and ●) of a single main cylinder increase mildly from 0.23 to 0.4 for Reynolds numbers between 80 and 300. These results agree well with those of Hoerner (1957). The slight increase in the viscous drag on a single cylinder is due to the large velocity gradient at the walls as the Reynolds number increases.

When the control cylinders are placed at $x/D = 0.5$ and $y/D = \pm 0.6$, the total drag coefficient ($\bar{C}_{dTc}$) of the cylinder system (i.e. the main cylinder and two control cylinders) decreases monotonously with increasing Reynolds numbers. Furthermore, the form and the total drag coefficients of the cylinder system form two nearly parallel curves as Reynolds number increases. This implies that the viscous drag coefficients are about 0.53 for all Reynolds numbers studied herein. For the cylinder system, it is impossible to accurately calculate the viscous drag for the main and the control cylinders separately based on the CV analysis; the detailed variations on the individual viscous drag of each cylinder are not yet understood well enough at present.

In Fig. 13, the total drag of the cylinder system is larger than that without control cylinders for $Re_D \leqslant 180$ because the increase of the viscous drag overwhelms the reduction of the form drag. However, for $Re_D > 180$, the total drag with control cylinders is smaller than the counterpart without control cylinders because the reduction of form drag is more significant than the increase of viscous drag.

4.7. Mechanism on wake modification and related lift alteration

The vortex formed asymmetrically (or in staggered arrangement) in the near wake can induce periodic lift force on the main cylinder. Therefore, both the loss of asymmetry of the flow structure in the near-wake and the significant delaying of vortex formation farther downstream are the main reasons for significant reduction of the fluctuating lift coefficient as Reynolds number increases from 80 to 300.

The vortex formation length is analyzed in Figs. 14 and 15. In the inset of Fig. 14, the new coordinate system X_1 and Y_1 is centered at the rear stagnation point S1. Here X_{Bomax} and U_{Bomax} denote respectively the location and the magnitude of the maximum mean velocity of the reversed flow occurred at the wake centerline. The length L_{fo}
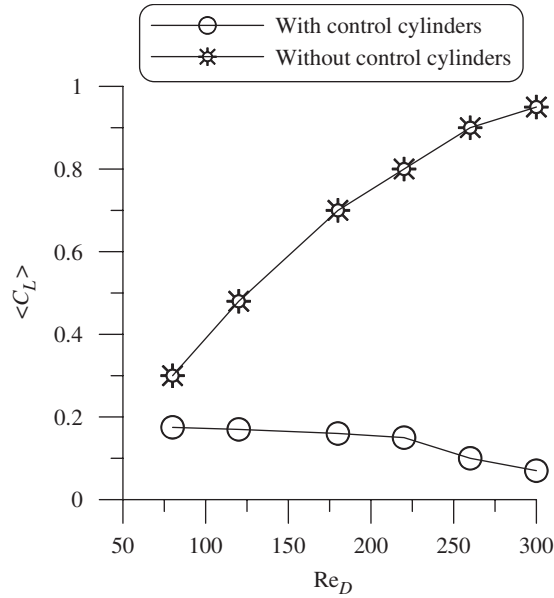
Fig. 12. Variations of fluctuating lift coefficients with and without control cylinders when the Reynolds number changes from 80 to 300.
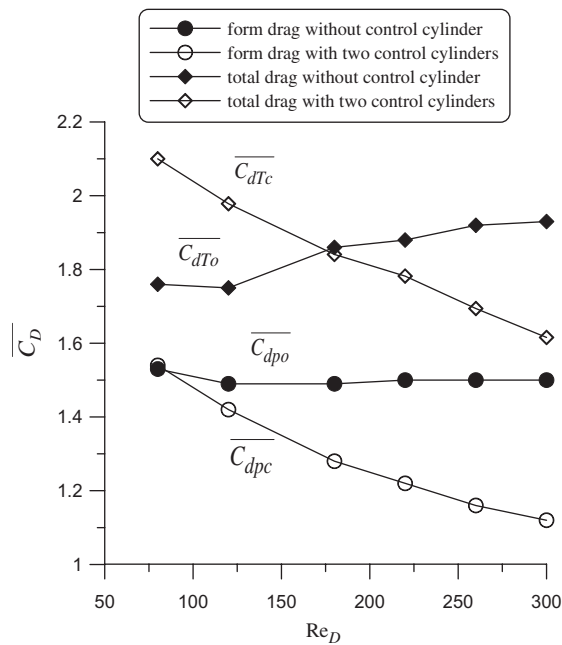

Fig. 13. Total and form drag coefficients variations for the cases with and without control cylinders as the Reynolds number ranges from 80 to 300.

represents the mean streamwise distance between the saddle points S1 and S2 and is defined as the vortex formation length (Bearman, 1965) for the case without control cylinders. Surprisingly, all the nondimensional velocity profiles in Fig. 14 collapse into a single curve. This implies that the length L_{fo} of the recirculation region behind the main cylinder is an important length scale regardless of the variations of Reynolds number between 80 and 300. On the left column of Fig. 9, the shorter the length L_{fo}, the higher is the shedding frequency behind the main cylinder. Therefore, the length L_{fo} is scaled with the shedding frequency and inversely with the wavelength of the vortex street.
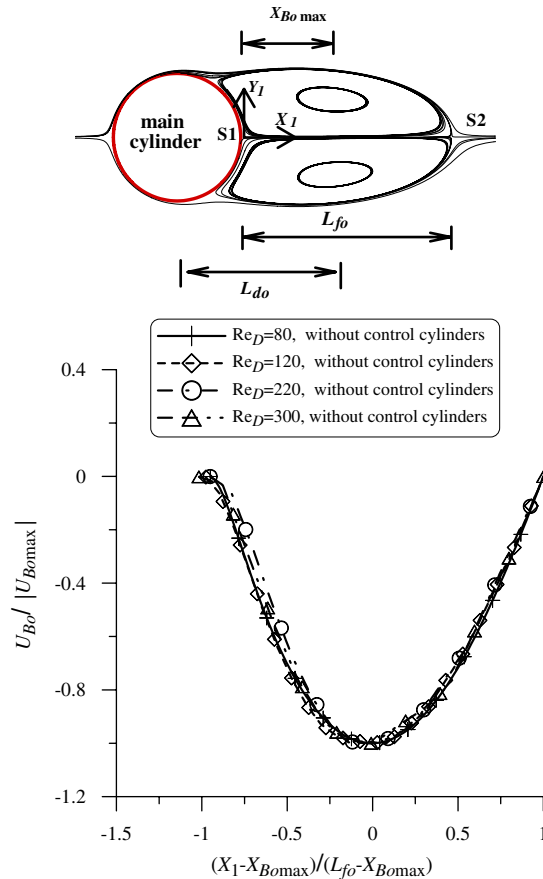
Fig. 14. Streamwise variations of the mean velocity of the reversed flow along the wake centerline when the Reynolds numbers change from 80 to 300. The parameters are defined in the inset on the top for the case without control cylinders.

For the case with two control cylinders (Fig. 15), the origin of the new coordinate is shifted to the saddle point S3, and the streamwise distance between saddle point S3 and S2 is referred as L_{fc}. In Fig. 15, only part of each curve collapses into a single nondimensional curve. The collapsed part of each curve coincides well with the recirculation region. Obviously, the length L_{fc} between saddle points S3 and S2 is also an important length scale for the wake flow when two control cylinders are applied. The noncollapsed part corresponds to the region between the saddle points S1 and S3 where the vorticity depletion region resides. In the central part of the vorticity depletion region, all the velocity vectors are moving downstream without flow reversal for all the Reynolds numbers studied. Therefore, the region between S3 and S1 is really nothing to do with the vortex formation. In the present study, the vortex streets are not significantly changed. The shedding frequencies are reduced only slightly relative to their no-control counterpart, so is the length L_{fc}, only slightly longer than L_{fo}, at each Reynolds number. It is evident in Fig. 15 that the shedding frequency is actually scaled with the length L_{fc}, and it has nothing to do with the distance between S1 and S3 when the two control cylinders are present.

On the other hand, the vortex formation distance (L_d) is defined as the streamwise distance between the centers of the main cylinder and the recirculation region shown in Figs. 14 and 15. For the cases of a single cylinder (left column of Fig. 9), the vortex formation length L_{fo} behind the main cylinder becomes short when the Reynolds number increases from 80 to 300. This variation trend is in accordance with the previous literature (Bearman, 1965; Griffin, 1995). So is the distance L_{do}. Therefore, in Fig. 11(a), large fluctuating magnitudes of C_p on the main cylinder are primarily caused by both the increasing peak values of $\tilde{u}_{r.m.s.}$ and the decreasing distance L_{do} as the Reynolds number increases from 80 to 300. Similarly, as the Reynolds number increases, smaller magnitudes of C_p in Fig. 11(b) are caused primarily by significant downstream movement of the vortex formation distance (L_{dc} in Fig. 9(b)) behind the main cylinder and small peak value of $\tilde{u}_{r.m.s.}$ (Fig. 10(d)) for the case with control cylinder. Thus, the distance L_{dc} is a suitable length that will be
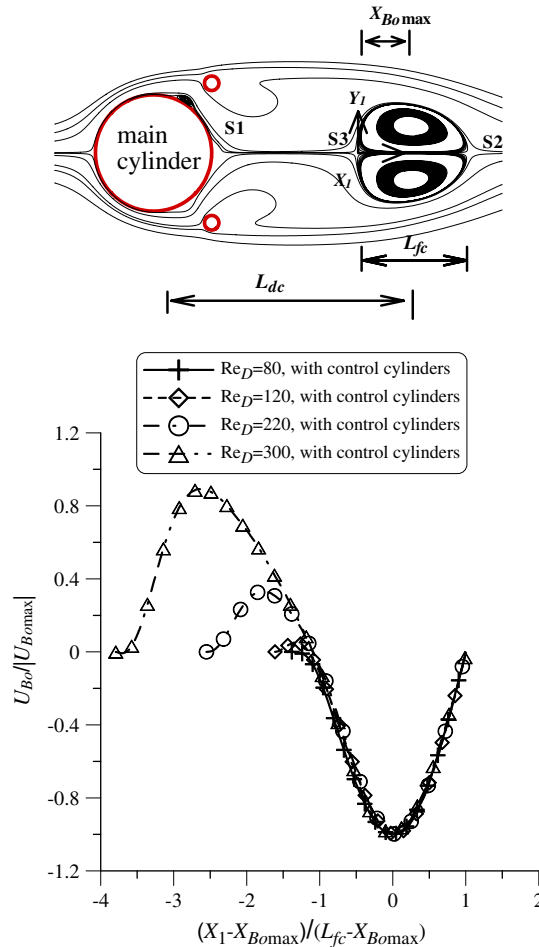
Fig. 15. Streamwise variations of the mean velocity of the reversed flow along the wake centerline when the Reynolds numbers change from 80 to 300. The parameters are defined in the inset on the top for the case with two control cylinders.

scaled with the magnitude of the induced surface pressure on the main cylinder when two control cylinders are placed at $x/D = 0.5$ and $y/D = \pm 0.6$.

5. Concluding remarks

A new mechanism, which can significantly reduce the fluctuating lift and the form drag on the main cylinder, is explored without completely suppressing the vortex street for $Re_D = 80$–300. In other words, by this control, the vortex street behind the main cylinder is still maintained but the fluctuating lift and the form drag on the main cylinder decreases monotonously with increasing Reynolds number.

In the present study, two small control cylinders, with diameter $d/D = 1/8$, are placed at $x/D = 0.5$ and $y/D = \pm 0.6$ and the Reynolds number is varied from 80 to 300. Obstruction of the small control cylinders to the incoming flow deflects part of the fluid to pass through the gaps between the main and small control cylinders. These streams not only eliminate the flow separation in the gap; they also create downstream advancing momentum in the immediate near-wake region. The advantages of this advancing momentum are twofold. First of all, as the Reynolds number increases from 80 to 300, the enhanced advancing momentum further minimizes the rotation rate of the fluid and increases the symmetry of flow structures in the near-wake region. It also delays the vortex formation farther downstream. This merit causes a monotonous decrease of the fluctuating lift coefficient on the main cylinder as the Reynolds number increases. Secondly, elimination of flow separation along the rear surface and merging of the two gap streams toward the wake

centerline of the main cylinder largely reduce the wake width. The second merit also reduces monotonously the form drag on the main cylinder as the Reynolds number changes from 80 to 300. As a whole, the total drag of the cylinder system is larger than that without control cylinders for $Re_D \leqslant 180$ because the increase of the viscous drag overwhelms the reduction of the form drag of the cylinder system. However, for $Re_D > 180$, the total drag of the cylinder system is smaller than the no-control counterpart because the reduction of form drag is more significant.

The results in the present study do not imply that the control efficiency is always better at Reynolds number 300 than at 80, because the location of optimal wake control is strongly dependent on the Reynolds number and the precise locations of the control cylinder. The apparent high control efficiency at Reynolds number 300 is due to the fact that the control cylinders are possibly placed near the contoured region of optimal efficiency. To perform efficient control of the surface loading (lift and drag) at higher Reynolds numbers, the optimal location of the control cylinder must be carefully studied in advance.

References

Bearman, P., 1965. Investigation of the flow behind a two-dimensional model with blunt trailing edge and fitted with splitter plate. Journal of Fluid Mechanics 21, 241–257.

Berger, E., 1967. Suppression of vortex shedding and turbulence behind oscillating cylinders. Physics of Fluids Series A 10, S191–S193.

Blevins, R.D., 1985. The effect of sound on vortex shedding from cylinders. Journal of Fluid Mechanics 161, 217–237.

Eisenlohr, H., Eckelmann, H., 1989. Vortex splitting and its consequences in the vortex street wake of cylinders at low Reynolds number. Physics of Fluids Series A 1, 189–192.

Ferziger, J.H., Peric, M., 1996. Computational Methods for Fluid Dynamics. Springer, Berlin.

Fluent 6.1, 2005. User's Manual. Fluent Inc.

Griffin, O.M., 1995. A note on bluff body formation. Journal of Fluid Mechanics 284, 217–224.

Hoerner, S.F., 1957. Fluid-Dynamic Drag, second ed. Midland Park, New Jersey.

Huner, B., Hussey, R.G., 1977. Cylinder drag at low Reynolds number. Physics of Fluids 20, 1211–1218.

Kuo, C.H., Jeng, W.I., 2003. Lock-on characteristics of a cavity shear layer. Journal of Fluids and Structures 18, 715–728.

Kim, S.J., Lee, C.M., 2001. Control of flows around a circular cylinder: suppression of oscillatory lift force. Fluid Dynamics Research 29, 47–63.

Lange, C.F., Durst, F., Breuer, M., 1998. Momentum and heat transfer from cylinders in laminar cross flows at $10^{-4} \leqslant Re \leqslant 200$. International Journal of Heat and Mass Transfer 41, 3409–3430.

Lecordier, J.C., Hamma, L., Parantheon, P., 1991. The control vortex shedding behind heated cylinders at low Reynolds numbers. Experiments in Fluids 10, 224–229.

Nakano, M., Rockwell, D.O., 1991. Destabilization of the Karman vortex street by frequency-modulated excitation. Physics of Fluids Series A 3 (5), 723–725.

Nigim, H.H., Batill, S.M., 1997. Flow about cylinders with surface perturbations. Journal of Fluids and Structures 11, 893–907.

Patankar, V.S., Spalding, D.B., 1972. A calculations procedure for heat, mass and momentum transfer in three-dimensional parabolic flows. International Journal of Heat and Mass Transfer 15, 1787–1806.

Perry, A.E., Chong, M.S., Lim, T.T., 1982. The vortex-shedding process behind two-dimensional bluff bodies. Journal of Fluid Mechanics 116, 77–99.

Roshko, A., 1955. On the wake and drag of bluff bodies. Journal of Aeronautical Science 22, 124–132.

Roussopoulos, K., 1993. Feedback control of vortex shedding at low Reynolds numbers. Journal of Fluid Mechanics 248, 267–296.

Strykowski, P.J., Sreenivasan, K.R., 1990. On the formation and suppression of vortex shedding at low Reynolds numbers. Journal of Fluid Mechanics 218, 71–107.

Suryanarayana, G.K., Pauer, H., Meier, G.E.A., 1993. Bluff-body drag reduction by passive ventilation. Experiments in Fluids 16, 73–81.

Tokumaru, P.T., Dimotakis, P.E., 1991. Rotary oscillation control of a cylinder wake. Journal of Fluid Mechanics 224, 77–90.

Williamson, C.H.K., Brown, G.L., 1998. A series in $1/\sqrt{Re_D}$ to represent the Strouhal–Reynolds number relationship of the cylinder wake. Journal of Fluids and Structures 12, 1073–1085.

Zdarvkovich, M.M., 1977. Review of flow interference between two circular cylinders in various arrangements. ASME Journal of Fluids Engineering 99, 618–633.

Zdravkovich, M.M., 1997. Flow Around Circular Cylinders, vol. 1: Fundamentals. Oxford University Press, New York.

Zhou, Y., Antonia, R.A., 1992. Convection velocity measurements in a cylinder wake. Experiments in Fluids 13, 63–70.